Ab initio Structure Determination of $Mg_{10}Ir_{19}B_{16}$

Qiang Xu,*[,†] T. Klimczuk,[‡,§] Ton Gortenmulder,[||] Jacob Jansen,[†] M. A. McGuire, R. J. Cava,[‡] and Henny W. Zandbergen[†,‡]

National Centre for HREM, Kavli Institute of Nanoscience, Delft University of Technology, 2628 CJ Lorentzweg 1, Delft, The Netherlands, Department of Chemistry, Princeton University, Princeton, New Jersey 08540, Faculty of Applied Physics and Mathematics, Gdansk University of Technology, Narutowicza 11/12, 80-952 Gdansk, Poland, and van der Waals-Zeeman Institute, University of Amsterdam, Amsterdam, The Netherlands

Received February 24, 2009

The ab initio structure determination of a novel unconventional noncentro-symmetric superconductor $Mg_{10}Ir_{19}B_{16}$ ($T_c = 5$ K) has been performed using a method that involves a combination of experimental data and calculations. Electron diffraction, X-ray powder diffraction, phase estimation routines, quantum mechanical calculations, high-resolution electron microscopy, and structural chemistry arguments are used. With the strengths of different methods used to eliminate the ambiguities encountered in others, the complete structure, including a very light B atom, has been determined with a high accuracy from impure polycrystalline powder samples, which suggests that the type of analysis described may be used to successfully address other similar intractable problems. The solved structure of $Mg_{10}Ir_{19}B_{16}$ shows a complex nature that irregular coordination environments preclude a conversional description of compact packing of coordination polyhedra; however, it can be easier understood as ordered in an onion-skin-like series of nested polyhedra.

Introduction

Compounds based on light elements are expected to be favorable in conventional electron−phonon coupled superconductivity because of the correspondingly high phonon frequencies they display. Therefore, such superconducting compounds have been of interest the past five years, e.g., MgB_2,[1] $MgCNi_3$,[2] C_6Yb, and C_6Ca.[3] Recently, a novel light-element-based ternary intermetallic superconductor $Mg_{10}Ir_{19}B_{16}$ ($T_c = 5$k) was synthesized. This material has a body-centered cubic crystal structure with a large unit cell, $a = 10.568$ Å, and consequently, a complex formula. Our previous research indicates that this compound is one of the rare examples of a noncentrosymmetric superconducting material (space group $I\bar{4}3m$).[4] To understand the physical properties and to know the exact composition of the superconducting phase, the detailed crystallographic studies are required. However, the structure determination of light-element-based superconducting materials is not easy using standard X-ray diffraction methods for two reasons. First, in the early stages of searching for new compounds, a reaction mixture will be often multiphase, complicating the interpretation of X-ray powder diffraction data. Second, light atoms scatter X-rays much less than heavy elements and so in the presence of heavy atoms the contribution of light elements to the intensities in the X-ray diffraction pattern will be quite small. Quantitative electron diffraction does not have these restrictions. Electron diffraction can be recorded from local sample areas (easily less <10 nm) using a nano probe, which allows one to select a single-phase area for study. Moreover, the dynamical diffraction effect makes electron diffraction sensitive to light atom positions, as explained further in the text. It has been shown that electron crystallography can be applied successfully to structure determination.[5−8] Whereas ab initio structure determination from X-ray single-crystal diffraction data is standard procedure, this is not yet the case for electron diffraction data because of dynamical scattering effects. Therefore, a different kind of ab initio analysis of the data is required.

Here we report the ab initio structure determination of the novel superconductor, $Mg_{10}Ir_{19}B_{16}$. By combining the use of high-resolution electron microscopy, quantitative electron diffraction, phase estimation routines, X-ray powder diffraction, and first-principle calculations deliberately, the complete crystal structure of this compound including B atoms was successfully determined with high accuracy from the impure polycrystalline powder sample. Although the local coordina-

* Corresponding author. Qiang Xu. E-mail: q.xu@tudelft.nl. Tel: 31-15-2781201. Fax: 31-15-2786600.
† Delft University of Technology.
‡ Princeton University.
§ Gdansk University of Technology.
|| University of Amsterdam.

(1) Nagamatsu, J.; Nakagawa, N.; Muranaka, T.; Zenitani, Y.; Akimitsu, J. *Nature* **2001**, *410*, 63.
(2) He, T.; Huang, Q.; Ramirez, A. P.; Wang, Y.; Regan, K. A.; Rogado, N.; Hayward, M. A.; Haas, M. K.; Slusky, J. J.; Inumara, K.; Zandbergen, H. W.; Ong, N. P.; Cava, R. J. *Nature* **2001**, *411*, 54.
(3) Weller, T. E.; Ellerby, M.; Saxena, S. S.; Smith, R. P.; Skipper, N. T. *Nat. Phys.* **2005**, *1*, 39–41.
(4) Klimczuk, T.; Xu, Q.; Morosan, E.; Thompson, J. D.; Zandbergen, H. W.; Cava, R. J. *Phys. Rev. B* **2006**, *74*, 220502.
(5) Zandbergen, H. W.; Andersen, S. J.; Jansen, J. *Science* **1997**, *277* (5330), 1221.
(6) Zandbergen, H. W.; Jansen, J. *J. Microsc.* **1998**, *190* (1−2), 222.
(7) Chen, J. H.; Costan, E.; van Huis, M. A.; Xu, Q.; Zandbergen, H. W. *Science* **2006**, *312* (5772), 416.
(8) Xu, Q.; Klimczuk, T.; Jansen, J.; Cava, R. J.; Zandbergen, H. W. *Chem. Mater.* **2006**, *18*, 4585–4591.

10.1021/cm9005458 CCC: $40.75
Published on Web 05/11/2009

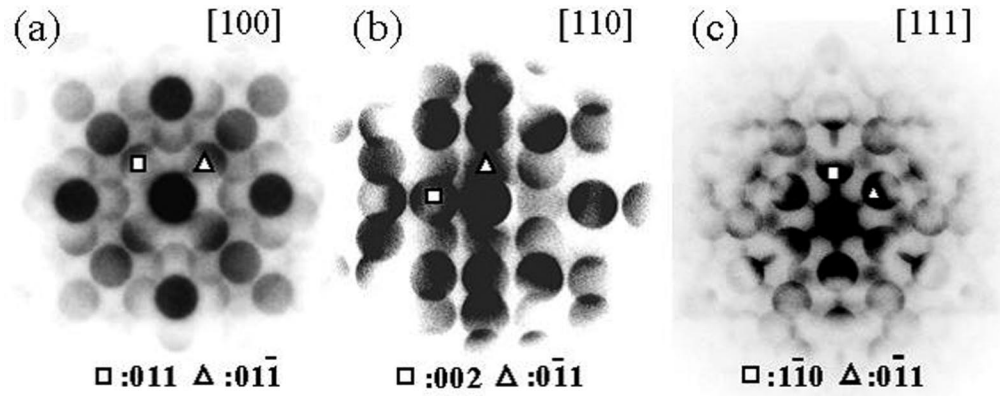

Figure 1. CBED pattern of Mg10Ir19B16 along (a) [100], (b) [110], and (c) [111] clearly show 4*mm*, *m*, 3*m* symmetry, respectively, which indicate the space group of the material is $I\bar{4}3m$.

tion environments of the atoms are irregular, the whole structure is highly ordered and capable of being interpreted in an alternative way, onionskin-like series of nested polyhedra. The success of using the methods in the current, complex case argues that the type of analysis described may be used to successfully address similar previously intractable structure problems.

Experimental Section

The synthesis of the samples in the Mg−Ir−B chemical system and the isolation of the superconducting phase are described in detail elsewhere.[4] The sample studied here had nominal composition $Mg_{12}Ir_{19}B_{19}$ and was known from X-ray powder diffraction analysis to contain about 5% of a foreign phase in addition to the superconductor. Powder X-ray diffraction (XRD) analysis was performed with Cu Kα radiation on a diffractometer equipped with diffracted beam monochromator. The X-ray diffraction pattern was analyzed using the refinement program GSAS.[9,10]

Electron microscopy analysis was performed with a Philips CM300T with a LaB_6 gun for the determination of the unit cell, and a Philips CM300UT electron microscope with a field emission gun, operated at 300 kV, and a link with an EDX element analysis system for HREM recording. The information limit of this microscope is 0.12 nm. High-resolution images were recorded with a 1024^2 pixel (24 μm × 24 μm) slow scan CCD camera (Tietz). For through-focus exit wave reconstruction (TF-EWR), a series of 20 HREM images were recorded with focus increments of 4.8 nm. Exposure times were 0.5−1.0s per HREM image. Electron diffraction was recorded on image plates with spot sizes less than 10 nm. Exposure times ranged from 1−3s (condenser aperture 10 μm) for the diffraction patterns used for structure refinement and 15−30s (condenser aperture 70 μm) for the convergent beam electron diffraction (CBED) pattern used for space group determination.

Crushing the sample did not yield areas that were sufficiently electron transparent, probably because of the high sample hardness in combination of the small grain size of $Mg_{10}Ir_{19}B_{16}$. An alternative sample preparation method was therefore used, as described elsewhere.[11]

Composition analysis was carried out using EPMA. The samples for EPMA were prepared in a similar fashion as for TEM.[11] EPMA by wavelength-dispersive X-ray spectroscopy (WDX) was performed with a JEOL 8621S microprobe. By SEM-imaging, suitable parts on the surface were selected. Pure Mg, Ir, and B were used as standards. Measured reflection lines and selecting crystals were, respectively: Mg Kα on TAP, Ir-Mα on TAP, and B−Kα on NSTE. The lines do not suffer from overlap effects by either the primary lines of the other elements or their harmonics.

The formation enthalpies and atomic position relaxations of the possible structure models (i.e., those with different in B positions) were calculated using the Vienna ab initio simulation package VASP code[12−14] with with the efficient US pseudopotentials and the Generalized Gradient Approximation (GGA).[15,16] For all structures, the Monkhorst-Pack *k*-point grid was chosen as 2 × 2 × 2 and the energy cutoff as 400 eV. The low accuracy setting was chosen for the ionic relaxation of B positions, while the other metal atoms were fixed (EDIFF = 1E-2, EDIFFG = −0.1). The high accuracy setting (EDIFF = 1E-4, EDIFFG = −0.01) was chosen for ionic relaxation of all atom positions in the final structure model.

Structure Refinement

1. Determination of Cell Parameters and Space Group. The initial cell parameters were obtained a using tilt series of electron diffraction patterns. A thin single crystal was selected and tilted over a large angular range of 60° about one short reciprocal vector (which was determined to be the (110) reflection after full analysis). From the recorded electron diffraction patterns for major zones, and the corresponding tilt angles, the reciprocal lattice was constructed, giving the approximate lattice parameters: cubic structure, a = 10.7 Å. The observed reflection conditions are *hkl*: $h+k+l = 2n$, corresponding to an *I* centered cubic Bravais lattice. Convergent beam electron diffraction (CBED) patterns along the [100], [110], and [111] zone axes clearly show the symmetries 4*mm*, *m*, and 3*m*, respectively (see Figure 1). It can therefore be concluded from the CBED results that the space group of MIB is $I\bar{4}3m$.[17,18] Using this space group

(9) Larson, A. C. and Von Dreele, R. B. *General Structure Analysis System (GSAS)*; Report LAUR 86−748; Los Alamos National Laboratory: Los Alamos, NM, 2000.
(10) Toby, B. H. *J. Appl. Cryst.* **2001**, *34*, 210–213.
(11) Xu, Q.; Kumar, V.; kruijff, T.; Jansen, J.; Zandbergen, H. W. *Ultramicroscopy* **2008**, *109*, 8–13.
(12) Kresse, G.; Furthmü ller, J. *Comput. Mater. Sci.* **1996**, *6*, 15.
(13) Kresse, G.; Furthmü ller, J. *Phys Rev B* **1996**, *54*, 11169.
(14) Kresse, G.; Hafner, J. *J. Phys.: Condens. Matter* **1994**, *6*, 8245.
(15) Blöchl, P. E. *Phys. Rev. B* **1994**, *50*, 17953.
(16) Perdew, J. P.; Burke, K.; Ernzerhof, M. *Phys. Rev. Lett.* **1996**, *77*, 3865.
(17) Tanka, M.; Saito, R.; Sekii, H. *Acta Crystallogr., Sect. A* **1983**, *39*, 357.
(18) Tanka, M. *Acta Crystallogr., Sect. A* **1994**, *50*, 261.

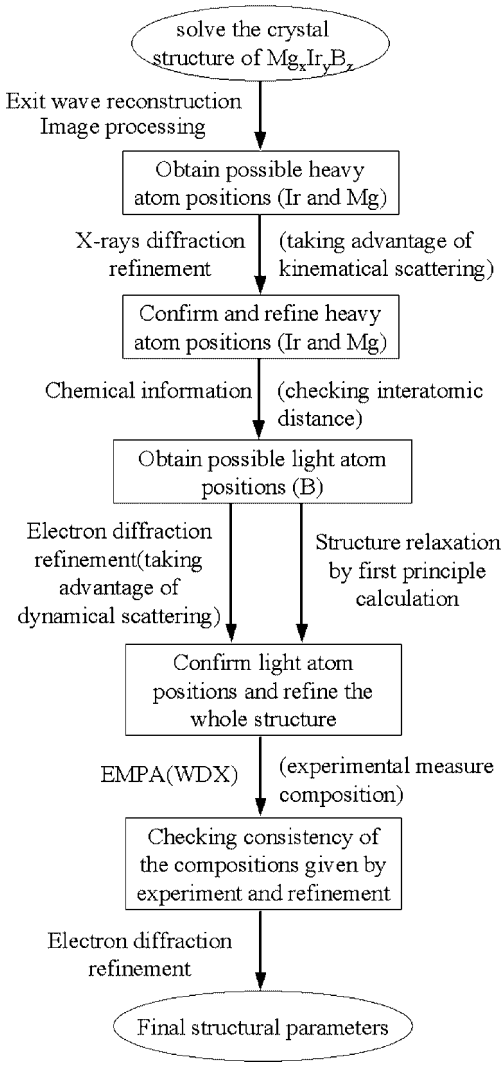

Figure 2. Illustration of the procedure for the determination of the atomic parameters for $Mg_{10}Ir_{19}B_{16}$.

and unit cell, all peaks in the powder X-ray diffraction pattern can be indexed. The unit cell of the phase was refined using a LaBail refinement of the powder X-ray pattern in GSAS, resulting in $a = 10.56782(4)$ Å.

2. Determination of Atomic Position Parameters. Before describing in detail the methods applied for deriving the crystal structure, we first describe in short the main purpose and procedure for all the methods employed (Figure 2). A starting model for the heavy atom positions was obtained by image processing of the exit wave reconstructed from a through focus series (analysis of image data) and direct methods (analysis of diffraction data). Assignment of correct heavy atom types (Ir and Mg) in those possible positions and refining the heavy atom position coordinates was done by XRD refinement. On the basis of the solved Ir and Mg positions, possible atom B positions were deduced by using crystallographic and chemical (i.e., B−Ir, B−Mg, and B−B interatomic distances) information. Next, the occupancies of these possible B positions and their coordinates were refined using electron diffraction refinement and first-principle calculations separately. Both of these refinements led to the same structure model for all atoms, and having a composition $Mg_{20}Ir_{38}B_{32}$ per cell ($Mg_{10}Ir_{19}B_{16}$). A composition measurement with EPMA was then performed, yielding a result consistent with the structure model. The final structure refinement was then carried out using electron diffraction data, providing all structure parameters.

3. Structure Information Obtained from Exit Wave Reconstruction. Possible heavy atom positions can be inferred from direct imaging, which is one advantage of electron crystallography. Direct interpretation of a HREM is normally hampered by image distortion because of lens imperfections. This problem can be overcome, however, by using exit wave reconstruction.[19] The amplitude and the phase of the exit wave along the [100] orientation was reconstructed using Trueimage software.[20] The display of the exit waves in Figure 3 is chosen such that atoms appear as white dots in the amplitude (shown in Figure 3a) as well as in the phase (shown in Figure 3b), provided the specimen thickness is thin enough. It can be seen in Figure 3a that on the edge of the sample the structure is not regular, and some parts is even close to amorphous, which we attribute to ion milling damage or the reaction with air. The part of the exit wave outlined by a white frame, however, shows sufficient crystallinity for detailed analysis. The exit wave was image processed as proposed by Zou[21] using the software VEC.[22] The image was symmetrized according to the spacegroup determined by CBED and the noise in the image was reduced by averaging over several unit cells (4×4). (Note that if the wrong symmetry is imposed (for instance, simply by a mistake in origin), then the falseness of the model will be evident in the subsequent structure refinement of the diffraction data.) By comparing the corrected exit wave, Figure 3e amplitude and Figure 3f phase, with hypothetical structure models, the possible heavy atom positions were generated (see Table 1 and the overlay on images e and f in Figure 3.

Before proceeding to the next step in the refinement, two cautions should be noted. First, some atom positions might be incorrect because of the overlapping of the atoms in the projection. Second, the reconstructed exit wave is still thickness-dependent, such that although the positions of the peaks in the exit wave do represent atom positions, the weight of these peaks might not reflect the scattering potential of these atoms because of the effects of dynamical scattering in electron diffraction (see Figure 4). Thus, although the possible positions of heavy atoms can be deduced from these images, the assignment of correct atomic types to these positions is still problematic at this stage. For this assignment, X-ray powder diffraction refinement was used.

4. Structure Refinement Using X-ray Powder Diffraction. X-ray diffraction was applied to determine the correct heavy atom positions. Among the three types of atoms contained in $Mg_{10}Ir_{19}B_{16}$, B is a very weak scatterer such that X-ray powder diffraction is almost insensitive to B

(19) Zandbergn, H. W.; Dyck, D. V. *Microsc. Res. Technol.* **2000**, *49*, 301.
(20) Kübel, C. Tang, D. Fliervoet, T. Thust, A., *Forschungszentrum Jülich, Trueimage Focus Series Reconstraction Package*; FEI Company: Hillsboro, OR, 2003.
(21) Xiaodong, Z. Electron Crystallography of Inorganic Structures−Theory and Practice. Ph.D. Thesis, 1995.
(22) Li, F.-h. *VEC, a Program for Visual Computing in Electron Crystallography*; Institute of Physics, Chinese Academy of Sciences: Beijing, China, 2000.

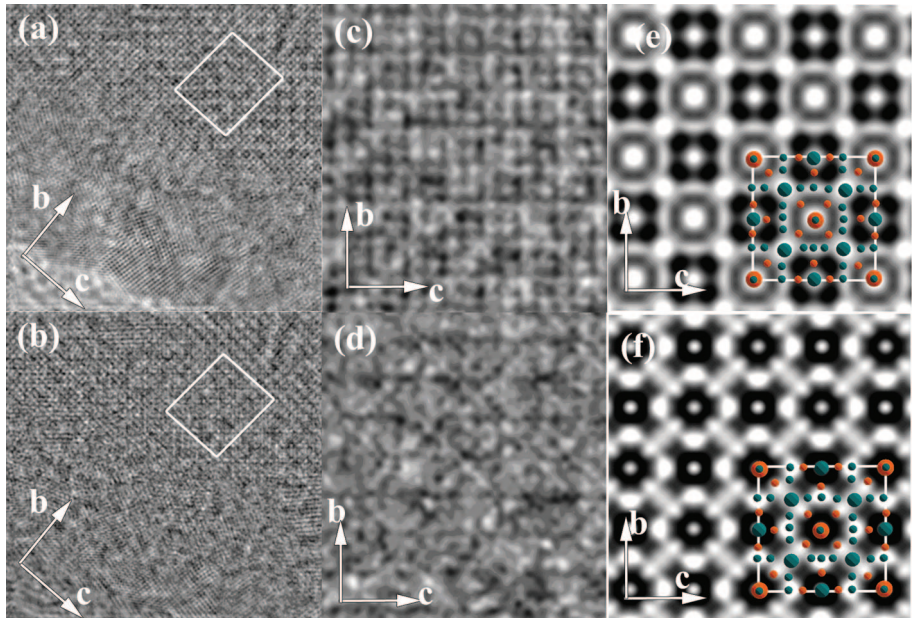

Figure 3. Exit wave (a) amplitude and (b) phase were reconstructed using a through focus series. The parts showing good crystallinity outlined by white frame are enlarged and shown in (c) and (d), respectively. Because of local misorientation and residual aberration, symmetries are generally lost in high-resolution imaging. To correct symmetry and improve signal-to-noise ratio, image processing was applied on (c) and (d) using software VEC,[20] resulting in a unit-cell-averaged and symmetry-corrected exit wave (e) amplitude and (f) phase. An overlay of atom positions as deduced from the exit wave is imposed on (e) and (f). Green and orange circles represent Ir and Mg atoms, respectively. Large circles represent situations where there are two Ir atoms or two Mg atoms per repeat unit along the projection direction. However, it should be noted that except for atom positions, all other information cannot be deduced from the image of the exit wave directly. Identity of the atoms was obtained from later X-ray diffraction refinement.

Table 1. Possible Heavy Atom Positions Derived from HREM and Direct Methods

	x	*y*	*z*	[a]
P1(2a)	0	0	0	(Ir)
P2(6b)	0	0.5	0.5	(X)
P3(8c)	0.25	0.25	0.25	(X)
P4(8c)	0.33	0.33	0.33	(X)
P5(12d)	0	0.25	0.5	(Ir)
P6(12e)	0	0	0.33	(Mg)
P7(12e)	0	0	0.25	(X)
P8(24 g)	0.1	0.25	0.25	(Ir)
P9(24 g)	0	0.33	0.33	(Mg)

[a] The corresponding atom types that are confirmed by XRD refinement are listed in the last column. (X) in this column indicates an incorrect atom position or an empty site; these incorrect atom positions were obtained because they overlap with other correct atom positions in projections. They were easily identified by the XRD refinement.

positions, given that other heavy atoms (Ir and Mg) are present. Ir is a much stronger scatterer than Mg, and the chemical studies indicated that content of Ir is higher in the superconducting phase. Thus, the X-ray powder diffraction pattern intensities are dominated by the Ir positions. Consequently, structure refinement based on X-ray powder diffraction can be used to determine the distribution of Ir and Mg from the atom positions suggested by the reconstructed exit wave. First, we did a refinement with Ir on all the suggested positions, yielding better atom positional coordinates. Next, we refined the occupancies of these "Ir" sites, enabling us successfully to distinguish the Ir positions and Mg positions, and to identify which of the positions suggested by the analysis of the exit wave are in fact empty (incorrect atom positions will give unstable positional parameters in the refinement or unphysical atomic parameters such as zero or negative occupancies or very high Debye−Waller factors). The refinement results for X-ray powder

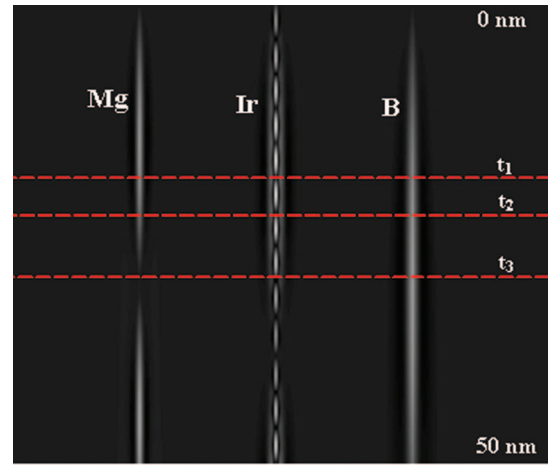

Figure 4. Simulation illustration of the electron channeling effect along different types of atomic columns by mapping the function $|\psi(R,z)|^2$, where Ψ is the function of the exit wave, R denotes the projected position of atom column (B, Ir, and Mg, respectively), and z is the penetration depth of incident electron from 0 nm (top) to 50 nm (bottom). As observed in the figure, the effective electron scattering power of an atom column oscillates with the penetration depth z (sample thickness). The amplitude of the oscillation is centered at the atom column position, resulting in that HREM can still reflect the atom positions in the projection up to a thickness much larger than that predicted by kinematical theory, but the values of amplitudes (or the peak intensities in the HREM) do not correspond to the kinematical scattering power of atoms anymore. For certain thicknesses, e.g., t1, t2, or t3, lighter atoms Mg or B column will scatter the electron more than the heavy atom Ir column will. Consequently, electron diffraction from the sample of these thicknesses will be more sensitive to the light atom positions.

diffraction are shown in Table 2 and Figure 5. The refinement gives the composition of heavy atoms to be $Mg_{20}Ir_{38}$ within the unit cell.

5. Using Chemical Information. B is such a light element that it is quite difficult to detect by HREM or X-ray powder

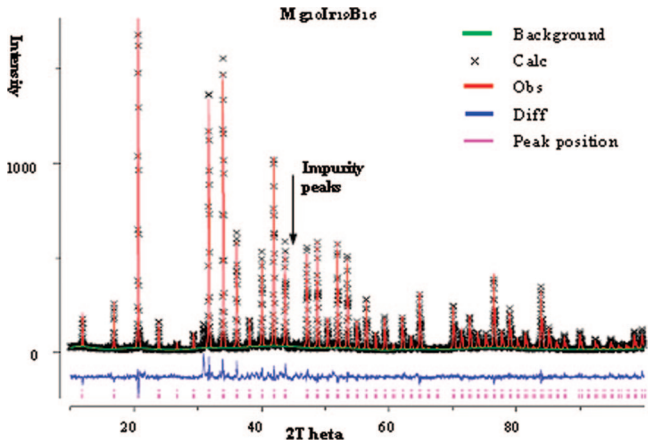

Figure 5. Rietveld refinement of powder X-ray diffraction pattern of the sample with nominal composition $Mg_{12}Ir_{19}B_{19}$. ($\chi^2 = 1.1$).

Table 2. Possible B Positions Deduced from Crystallographic and Chemical Information

B_1(8c)	B_2(24g)	B_3(24g)
(x_1,x_1,x_1) $x_1 = 0.11-0.12$	(x_2,y_2,y_2) $x_2 = 0.39-0.44$; $y_2 = 0.15-0.18$	(x_3,y_3,y_3) $x_3 = 0.15-0.16$; $y_3 = 0.09-0.08$

diffraction if heavy elements are also present.[23] To obtain possible starting models for the B positions, we used crystallographic and chemical information. Given the known Ir and Mg positions and the space group, interstitial sites suitable for placing B atoms were found by assuming a B to be in the center of vacant sites. A check was then performed on the interatomic distances to neighboring Ir and Mg atoms and nearby B atoms generated by the symmetry. In literature data, Ir−B, Mg−B, and B−B distances are found to be usually not less than 2.0, 2.3, and 0.7 Å, respectively. Using these interatomic distances as criteria, the following possible approximate B sites were obtained (see also Table 2): B_1 (0.11, 0.11, 0.11), B_2 (0.41, 0.16, 0.16), B_3 (0.15, 0.09, 0.09). The minimum distance between B_1 and B_3 positions is around 0.52 Å, which is too short. Thus only one of the two sites can be occupied, or partial occupancies have to occur. Only five possible combinations of B sites can be deduced for the structure of $Mg_{20}Ir_{38}B_z$: (1) only one B position at B_1; (2) only one B position at B_2; (3) only one B position at B_3; (4) two B positions at B_1 and B_2; (5) two B positions at B_2 and B_3. Using electron diffraction refinement combined with first-principle calculations, we determined the correct B positions.

6. Structure Refinement Using Electron Diffraction. To prove the correctness of the selected B positions and to refine the atom positions, we employed the least-squares refinement package MSLS.[24] This software takes dynamical electron diffraction into account explicitly. According to channeling theory,[25] dynamical scattering results in a focusing and subsequent defocusing of the part of the electron wave in a given atom column (see figure 4). This effect can be expressed by an effective column scattering power that oscillates as a function of the penetration depth of incident electrons. Although the relative scattering potentials of different columns will depend on thickness, the positions do not vary. For that reason, a HREM image can still reflect the atom positions up to a thickness much larger than that allowed for kinematical diffraction, yielding peaks that are real atom positions, (For instance, the projected Ir positions from complete structure refinement differ only 0.3 Å from the positions determined from th HREM data) but the amplitudes of these peaks will no longer correspond to the scattering potential of the atoms to which the columns are composed. As shown in Figure 4, the lighter-atom Mg and B columns scatter more than the heavy atom Ir column for certain thicknesses, e.g., t_1, t_2, or t_3. Consequently, electron diffraction data from the sample at these thicknesses are more sensitive to the lighter atoms. Thus by combining a series of electron diffraction data sets for different thicknesses and different zones, all atom positions can be refined simultaneously, with dynamical effects taken into account.

Refinements with the MSLS software were performed using 12 data sets for different thicknesses and 3 different zones simultaneously. Refinement of the positions and occupancies of all three possible B positions shows that the model with B atoms at the B_1 and B_2 positions (see Table 3) give the lowest R value. Subsequent refinement of all atom parameters resulted in positions of Ir and Mg in good agreement with those obtained by XRD refinement (see Table 4), with normal thermal parameters and interatomic distances, including those for B (see Table 7). The unit-cell content was thus found to be $Mg_{20}Ir_{38}B_{36}$, yielding a formula for the superconductor of $Mg_{10}Ir_{19}B_{16}$.

7. Structure Refinement Using First-Principle Calculations. The atom positions of $Mg_{10}Ir_{19}B_{16}$ can be also refined using first-principle calculations. Comparing to electron and X-ray diffraction refinements, in which the R value ($R = \Sigma_g(I_{obsd} - I_{calcd})^2/\Sigma_g I_{obsd}^2$) is minimized, a structure relaxation by first-principle calculations is based on the minimization of the forces between the atoms by relaxation of the atom positions (and, if wanted, the unit-cell dimensions). An advantage of first-principle calculations is that they are also sensitive to light atom positions (because the interatomic forces are primarily set by only the valence electrons). Moreover, apart from the relaxation of atom positions, such calculations also allow for a comparison of the stabilities of postulated models (such as possible B positions), because the calculated formation enthalpy reflects the thermodynamic stability of the system. Because this method provides a completely different weighting criterion for choosing the correct B positions, it is complementary to diffraction techniques. The formation enthalpies of $Mg_{20}Ir_{38}B_z$ with different B position configurations (see Table 3) were calculated with fully relaxed atom positions using the ab initio VASP code. The calculations show that the configuration in which B occupies the B1 and B2 positions gives the lowest enthalpy of formation, indicating that this configuration is highly probable. However, without knowledge of the exact composition, a direct selection of the right model only based on the gain of energy may be not possible and not correct from these first-principle calculations alone (For instance, both graphite and diamond exist in nature, but

(23) Hofmann, K.; Albert, B. *Chem. Phys. Chem* **2002**, *3* (10), 896.
(24) Jansen, J.; Tang, D.; Zandbergen, H. W.; Schenk, H. *Acta Crystallogr., Sect. A* **1998**, 91.
(25) Van Dyck, D.; Op de Beeck, M. *Ultramicroscopy* **1996**, *64*, 99–107.

Table 3. *R*-Values of the Electron Diffraction Refinements and Calculated Total Enthalpies for the Different B Configurations Listed in Table 2

	B_1(8c)	B_2(24g)	B_3(24g)	$B_1 + B_2$ (32)	$B_2 + B_3$(48)*
R value	0.079	0.072	0.084	0.056	0.064
total enthalpy (ev)	5.25×10^{1}	1.06×10^{1}	7.57×10^{1}	-7.76×10^{0}	-8.70×10^{0}
total enthalpy/atom (ev)	7.95×10^{-1}	1.15×10^{-1}	9.23×10^{-1}	-8.63×10^{-2}	-8.21×10^{-2}
deviation of heavy atoms (pm)	1.07×10^{1}	1.02×10^{1}	7.69×10^{1}	1.40×10^{0}	5.61×10^{1}

* The calculation for configuration of $B_2 + B_3$ by VASP is unstable (total magnetic moment fluctuates a lot). Though the total enthalpy of this configuration is still a negative value and close to that of $B1 + B_2$, the large deviation of heavy atoms away from the diffraction refinement positions indicates that this configuration is not favorable.

Table 4. Fractional Coordinates (*x*, *y*, *z*) of Atom Positions in Space Group $I\bar{4}3m$ Refined by Electron Diffraction (ED) and the Deviations (Δx, Δy, Δz) in Picometers from These Positions in the Refined Positions Using X-ray Diffraction (XRD) Data and the First Principle Calculations (QM)

	ED				XRD			QM		
	x	*y*	*z*	*B* (Å^2)[a]	Δx	Δy	Δz	Δx	Δy	Δz
Ir1	0	0	0	3.04(3)	0	0	0	0	0	0
Ir2	0	0.25	0.5	0.99(1)	0	0	0	0	0	0
Ir3	0.07025(5)	0.25248(4)	0.25248	1.19(1)	4	−0	−0	−2	−2	−2
Mg1	0.3331(2)	0.3331	0.3331	0.15(2)	8	8	8	−1	−1	−1
Mg2	0	0	0.3473(3)	0.15(2)	0	0	−6	0	0	1
B1	0.1127(3)	0.1127	0.1127	0.08(9)				−2	−2	−2
B2	0.1639(2)	0.1639	0.4140(3)	0.48(6)				−1	−1	−3

[a] *B* positions are not given in the XRD result because they cannot be refined by XRD because of much small scattering power of *B* to X-ray.

Table 5. Comparison of the Experimental Composition Determined by EPMA and the Calculated Compositions for Different B Configurations

	Mg (%)	Ir(%)	B(%)
B1	30.30	57.58	12.12
B2	24.39	46.34	29.27
B3	24.39	46.34	29.27
B1 + B2	**22.22**	**42.22**	**35.56**
B2 + B3	18.87	35.85	45.28
experimental	**23.0(8)**	**41.6(9)**	**35.5(6)**

diamond is less stable than graphite from a thermodynamic viewpoint). A better way might be using a comparison between the refined Ir and Mg positions obtained by energy minimization and those of the MSLS refinement, which does allow the selection of the right model. Note that in the relaxations of the structures listed in Table 3, all the Ir and Mg atoms were fixed to the positions determined by X-ray diffraction refinement and only B atoms were allowed to shift. This constraint effectively avoids possible correlations between B, Mg, and Ir positions. After the optimal B configuration was determined (B_1 and B_2 sites), all atoms were then relaxed simultaneously. The final atom positions are listed in Table 4. The relaxed unit cell dimension is $a = 10.574$ Å, only 0.06% larger than the experimental one obtained from X-rays refinement.

8. Composition Analysis (EPMA). The composition of the material, determined with electron and X-ray diffraction and first-principle calculations to be $Mg_{10}Ir_{19}B_{16}$ was confirmed by electron probe microanalysis (EPMA).[26] The EPMA results are in very good agreement with the model obtained from the diffraction refinements and first-principle calculations, as can be seen in Table 5.

9. Final Structure Refinement Using Electron Diffraction. The refinement results of X-ray diffraction, electron diffraction, and first-principle calculations are consistent (see Table 4), differing in atom positions by less than 0.08 Å. Furthermore, the elemental composition of the refined structure is in good agreement with the EPMA measured composition shown in Table 5. To check whether the slight difference in the results obtained from electron diffraction and first-principle calculations is due to a false minimum in the data refinement, we performed a refinement with the atom positions as determined by first-principle calculation as starting model. This refinement led to the same positions as obtained previously for the electron diffraction refinements, suggesting that the global minimum had already been reached. The results of the refinement as well as data on the electron diffraction patterns (e.g., the number of reflections, refined crystal misorientations, and *R* values of each diffraction pattern) are listed in Table 6 and 7, respectively. The bond lengths are presented in Table 8.

Description of Structure

The coordination environments of all the atoms in $Mg_{10}Ir_{19}B_{16}$ (corresponding to the interatomic distances listed in Table 8 are shown in Figure 6. Ir1 and Ir2 are both coordinated to Mg and B in distorted tetrahedral arrangements. Ir2 is also in the plane of four coordinating Ir3 atoms. Like Ir1 and Ir2, Ir3 is also tetrahedrally coordinated to B, but is out of the plane of four coordinating Ir atoms and is bonded to four Mg atoms in an irregular geometry. Mg1 has triangular-prismatic coordination to six B atoms, is bonded to seven Ir atoms, and is just out of the plane of a triangle of three coordinating Mg2 atoms. Mg2 is in the planes of four coordinating B atoms and three coordinating Mg atoms and is bonded to eight Ir atoms in a distorted square-pyramidal arrangement. B atoms are in interstitial positions of the Ir and Mg network. The irregular coordination environments shown in Figure 6 attest to the complex nature of the crystal structure of $Mg_{10}Ir_{19}B_{16}$, and preclude the description of this structure by the conventional packing together of coordination polyhedra. The crystal structure of

(26) Wenzel, T.; Nickel, K. G.; Glaser, J.; Meyer, H.-J.; Eyidi, D.; Eibl, O. *Physica Status Solidi (a)* **2003)** , *198*, 374–386.

Table 6. Data on the Electron Diffraction Sets Used for the Structure Refinement of $Mg_{10}Ir_{19}B_{16}$ Listed in Table 7; Crystal Misorientation Is Given As the Position of the Projection of the Center of the Ewald Sphere in Miller Indices *h*, *k*, *l*[a]

			crystal misorientation			
zone	no. of obsd reflns	thickness (nm)	*h*	*k*	*l*	*R* value (%)
[100]	323	4.4(1)	0	1.8(1)	8.5(1)	5.6
[100]	290	7.2(1)	0	0.7(1)	−0.8(1)	5.8
[100]	312	15.3(1)	0	2.2(1)	0.0(1)	6.1
[100]	313	23.3(1)	0	0.2(1)	2.5(1)	9.7
[100]	365	38.5(1)	0.0	−0.1(1)	−0.1(1)	5.3
[110]	160	6.0(1)	0.3(1)	0.3(1)	−1.5(1)	7.3
[110]	211	7.7(1)	1.2(1)	1.2(1)	−1.8(1)	3.1
[110]	265	9.0(1)	0.5(1)	0.5(1)	−0.1(1)	2.6
[110]	244	22.4(1)	−1.4(1)	−1.4(1)	−2.2(1)	5.2
[110]	203	24.2(1)	−1.3(1)	1.3(1)	−0.7(1)	6.6
[111]	402	8.0(1)	−1.0(1)	0.4(1)	1.5(1)	4.5
[111]	504	22.7(1)	−6.5(1)	−2.9(1)	3.7(1)	4.9

[a] For simplicity, only one digit after the decimal was kept for sample thickness and misorientations, resulting in the standard deviations listed above being several orders larger than reality. The truncations induce only a 0.02% increase of the *R* value.

Table 7. Crystallographic Data for $Mg_{10}Ir_{19}B_{16}$ from Electron Diffraction with $a = 10.56782(4)$ Å and Space Group $I\bar{4}3m$[a]

	x	*y*	*z*	*B* (Å^2)	occ.
Ir1(2a)	0	0	0	3.04(3)	1
Ir2(12d)	0	0.25	0.5	0.99(1)	1
Ir3(24 g)	0.07025(5)	0.25248(4)	0.25248	1.19(1)	1
Mg1(8c)	0.3331(2)	0.3331	0.3331	0.15(2)	1
Mg2(12e)	0	0	0.3473(3)	0.15(2)	1
B1(8c)	0.1127(3)	0.1127	0.1127	0.08(9)	1
B2(24 g)	0.1639(2)	0.1639	0.4140(3)	0.48(6)	1

[a] $R = 5.6\%$.

Table 8. Selected Interatomic Distances

Ir1	B1	4×	2.063	(4)
Ir1	Mg1	4×	3.055	(3)
Ir2	B2	4×	2.157	(3)
Ir2	Ir3	4×	2.719	(1)
Ir2	Mg2	4×	3.096	(2)
Ir3	B2	1×	2.071	(3)
Ir3	B1	1×	2.137	(4)
Ir3	B2	2×	2.184	(3)
Ir3	Ir2	2×	2.719	(1)
Ir3	Ir3	2×	2.724	(1)
Ir3	Mg1	1×	2.814	(3)
Ir3	Mg2	2×	2.945	(1)
Ir3	Mg1	1×	3.028	(3)
Mg1	B2	3×	2.669	(4)
Mg1	Ir3	3×	2.814	(3)
Mg1	Ir3	3×	3.028	(3)
Mg1	Ir1	1×	3.055	(3)
Mg1	B1	3×	3.064	(4)
Mg1	Mg2	3×	3.140	(3)
Mg2	B2	2×	2.549	(3)
Mg2	Ir3	4×	2.945	(2)
Mg2	B1	2×	2.997	(5)
Mg2	Ir2	4×	3.096	(2)
Mg2	Mg1	2×	3.140	(3)
Mg2	Mg2	1×	3.227	(5)

this compound is most easily visualized by examining the Ir, Mg, and B sublattices separately.

Ir is the electronically active part of the structure, and thus the connectivity of its array is of particular interest. The Ir array is illustrated in Figure 7a. Ir2 are found at the vertices of cube-truncated octahedra. In this truncated octahedron, Ir2−Ir2 distances are 3.7 Å, significantly longer than the Ir−Ir bond length found in Ir metal (~2.7 Å). Each hexagonal face of the Ir2 cube truncated octahedron is decorated by an equilateral triangle of Ir3, with intratriangle Ir3−Ir3 bonds of 2.72 Å. Connectivity of the Ir network is realized through Ir2−Ir3 bonding at 2.72 Å. The Ir3 triangles

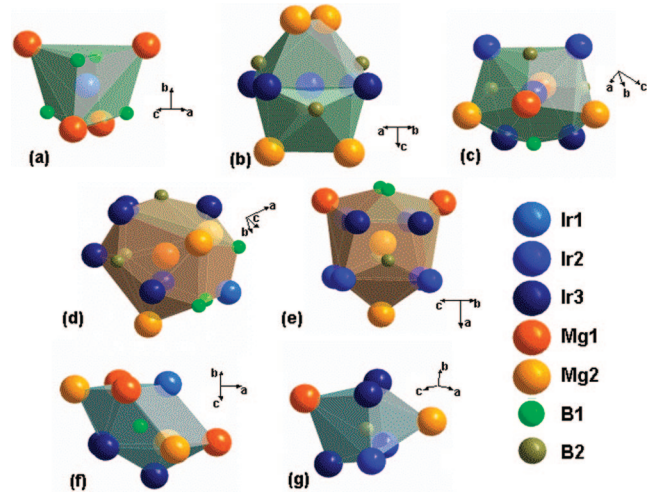

Figure 6. Coordination polyhedra of Ir, Mg, and B: (a) Ir1, (b) Ir2, (c) Ir3, (d) Mg1, (e) Mg2, (f) B1, and (g) B2. Ir, Mg, and B are depicted by large dark green, large orange, and small light green balls, respectively. Corresponding interatomic distances are listed in Table 8.

are alternatively puckered into and out of the Ir2 polyhedron along each κ direction. Ir1 atoms are not directly bonded to the Ir2−Ir3 network and reside at the centers of the Ir2−Ir3 polyhedra shown in Figure 7a.

We know of no other material that contains a network of a single element like that seen for Ir in $Mg_{10}Ir_{19}B_{16}$ (Figure 7a). However, similar structural features composed of two types of atoms can be found in other materials. Paladium and P atoms in $La_6Pd_6P_{17}$ form a network with P triangles decorating the faces of a cube truncated octahedron of Pd atoms.[27] In the mineral tetrahedrite $Cu_{12}Sb_4S_{13}$,[28] Cu atoms for a cube truncated octahedron, and S atoms form triangles decorating the hexagonal faces. However, neither of these compounds has the intratriangle bonds seen in the Ir3 units in $Mg_{10}Ir_{19}B_{16}$. In addition, the full Cu−S network in tetrahedrite involves bonding to other Cu and S atoms which reside inside of the cube truncated octahedron "cage", making a Cu−S sublattice significantly different than that shown in Figure 7a. Some similarity exists between the Ir2−Ir3 cage in $Mg_{10}Ir_{19}B_{16}$ and the Ga/Ge framework of the alpha form

(27) Jeitschko, W.; Hofmann, W. K. *J. Less-Common Met.* **1983**, *95*, 317–322.
(28) Pfitzner, A.; Evain, M.; Petricek, V. *Acta Crystallogr., Sect. B* **1997**, *53*, 337–345.

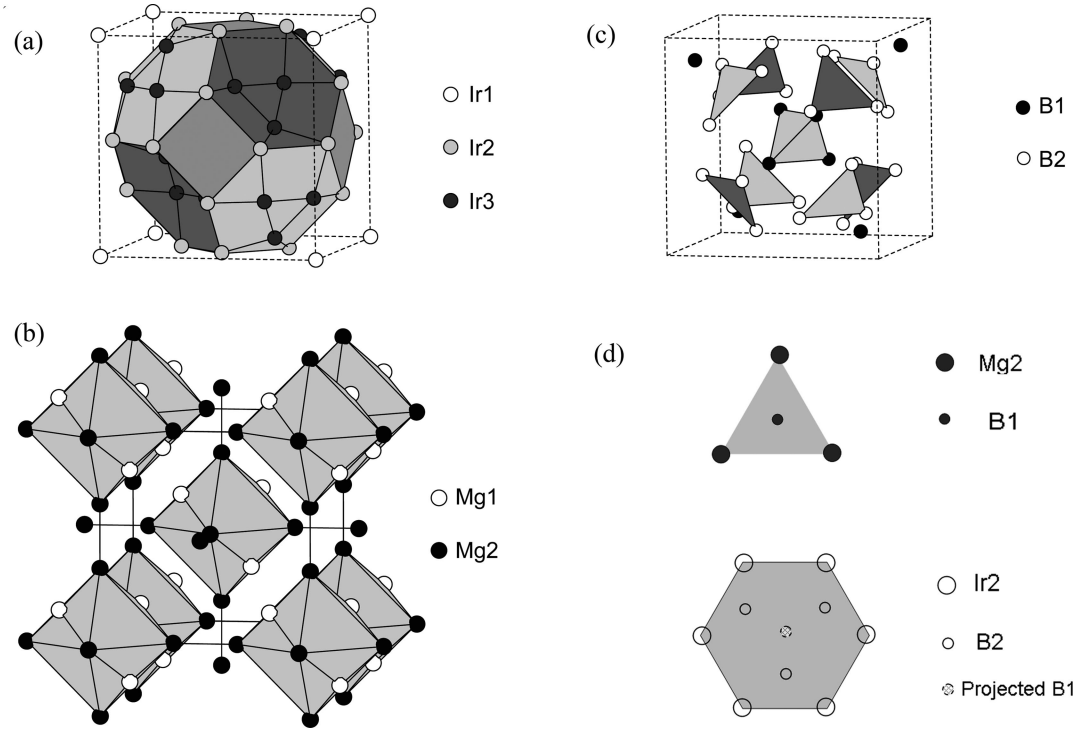

Figure 7. Crystal structure of $Mg_{10}Ir_{19}B_{16}$ viewed as individual Ir, Mg, and B sublattices. (a) The Ir network formed by Ir2−Ir3 and Ir3−Ir3 bonding and isolated Ir1 atoms. (b) Mg_{10} units formed by Mg1−Mg2 bonding joined into two interpenetrating simple cubic lattices through Mg2−Mg2 bonding. (c) The distribution of B atoms, with connections shown only to aid in visualization; there are no B−B bonds in $Mg_{10}Ir_{19}B_{16}$.

of the clathrate $Eu_8Ga_{16}Ge_{30}$.[29] However, bonding to other Ga/Ge atoms in $Eu_8Ga_{16}Ge_{30}$ results in a splitting of the "cage" shown in Figure 7a into four smaller cavities in which the Eu atoms reside.

The Mg network is shown in Figure 7b. Mg2 atoms form an octahedron about the unit cell origin, with Mg1 atoms capping four of the faces to form an Mg1 tetrahedron [d(Mg1−Mg2) = 3.14 Å, the Mg−Mg distance in Mg metal is 3.2 Å]. These units are joined to neighboring units through bonding between Mg2 atoms [d(Mg2−Mg2) = 3.23 Å], forming a three-dimensional Mg network. Body-centering then results in two interpenetrating simple cubic networks of Mg_{10} units, as shown in Figure 7b. Each Mg_{10} unit is encapsulated by an Ir polyhedron like that shown in Figure 7a. Mg2−Mg2 bonds connecting neighboring units penetrate the square faces of the Ir2 cube truncated octahedron. Sublattices like the Mg network shown in Figure 7b are also found in gamma-brass phases. For example, the sites occupied by Pd atoms in Pd_3Zn_{10} form a network identical to that shown in Figure 7b.[30]

Figure 7c shows the locations of the B atoms within the unit cell. We note that connections between B atoms in Figure 7c are meant only to aid in visualization; there are no B−B bonds in this compound (see Figure 6). B1 atoms form a tetrahedron surrounding the unit cell origin and each lies exactly at the center of the triangular face of Mg2. B2 atoms form triangular units perpendicular to the κ directions which lie exactly on the hexagonal faces of the Ir2 cube-truncated octahedron (Figure 7d).

The full structure is constructed by combining these three noncentrosymmetric sublattices. It is helpful to view the structure as an onion-skin-like series of nested polyhedra. Moving outward from Ir1, we find a B1 tetrahedron (Figure 7c), an Mg1 tetrahedron (Figure 7b), an Mg2 octahedron (Figure 7b), a tetrahedron of Ir3 triangles (Figure 7a), a cube of B2 triangles, and finally a cube-truncated octahedron of Ir1 (Figure 7a), which outlines the primitive unit cell. Because the center of symmetry is strongly broken by the Ir array, the origin of superconducting in the material can not be simply explained at this time. It may suggest that the combination of the lack of inversion symmetry, and the significant spin orbit coupling effect expected for Ir will lead to some unconventional character for the superconducting state.[31−34] Further property characterization would be of significant interest.

Conclusion

Employing novel combination of high-resolution electron microscopy, electron diffraction, powder X-ray diffraction, and total energy calculations, we have determined the crystal structure of the complex intermetallic superconductor $Mg_{10}Ir_{19}B_{16}$ with a high accuracy from impure polycrystalline powder samples. The success suggests that the type of analysis described may be used to address other similar intractable problems.

(29) Paschen, S.; Carrillo-Cabrera, W.; Bentien, A.; Tran, V. H.; Baenitz, M.; Grin′, Yu. N. *Phys. Rev. B* **2001**, *64*, 2144041–21440411.
(30) Edstroem, V.-A.; Westman, S. *Acta Chem. Scand.* **1969**, *23*, 279–285.
(31) Samokhin, K. V.; Zijlstra, E. S.; Bose, S. K. *Phys. Rev. B* **2004**, *69*, 094514.
(32) Frigeri, P. A.; Agterberg, D. F.; Koga, A.; Sigrist, M. *Phys. Rev. Lett.* **2004**, *92*, 097001.
(33) Samokhin, K. V. *Phys. Rev. Lett.* **2005**, *94*, 027004.
(34) Yuan, H. Q.; Agterberg, D. F.; Hayashi, N.; Badica, P.; Vandervelde, D.; Togano, K.; Sigrist, M.; Salamon, M. B. *Phys. Rev. Lett.* **2006**, *97*, 017006.

Although the local coordination environments of the atoms are irregular, the structure of $Mg_{10}Ir_{19}B_{16}$ can be simply described as a set of regular, nested Mg and Ir polyhedra, with B in interstitial positions. The center of symmetry is strongly broken by the Ir array. It may suggest that the combination of the lack of inversion symmetry, and the significant spin orbit coupling effect expected for Ir will lead to some unconventional character for the superconducting state.[31−34]

Acknowledgment. The authors acknowledge financial support from the European Union under the Framework 6 program under a contract for an Integrated Infrastructure Initiative, Reference 026019 ESTEEM. The work at Princeton was supported by the U.S. Department of Energy, Division of Basic Energy Sciences, Grant DOE-FG02-ER45706. Discussions with T. McQueen and G.C. Lau are gratefully acknowledged.

CM9005458